Control and Cybernetics

vol. **37** (2008) No. 4

Optimal design of stationary flow problems by path-following interior-point methods * †

by

Harbir Antil[1], **Ronald H.W. Hoppe**[1,2] **and Christopher Linsenmann**[1,2]

[1]Department of Mathematics, University of Houston
Houston, TX 77204-3008, USA
[2]Institute of Mathematics, University at Augsburg
D-86159 Augsburg, Germany
e-mail: harbir@math.uh.edu, hoppe@math.uni-augsburg.de,
linsen@math.uh.edu

Abstract: We consider the numerical solution of structural optimization problems in CFD where the state variables are supposed to satisfy a linear or nonlinear Stokes system and the design variables are subject to bilateral pointwise constraints. Within a primal-dual setting, we suggest an all-at-once approach based on interior-point methods. The discretization is taken care of by Taylor-Hood elements with respect to a simplicial triangulation of the computational domain. The efficient numerical solution of the discretized problem relies on path-following techniques, namely a continuation method with an adaptive choice of the continuation step size, a long-step path-following algorithm and a nonlinear version of Mehrotra's algorithm. The performance of the suggested methods is documented by several illustrative numerical examples.

Keywords: shape optimization, Stokes flow problems, path-following interior-point methods.

1. Introduction

Optimal design problems associated with fluid flow problems play a decisive role in a wide variety of engineering applications (see, e.g., Mohammadi and Pironneau, 2001, and the references therein). A typical example is to design the geometry of the container of the fluid, e.g., a channel, a reservoir, or a network of channels and reservoirs, in such a way that a desired flow velocity and/or pressure profile is achieved. The solution of the problem amounts to the minimization of an objective functional that depends on the so-called state

*The work has been supported by the NSF under Grant No. DMS-0511611 and Grant No. DMS-0707602 and by the Texas Learning and Computing Center TLC2.
†Submitted: May 2008; Accepted: September 2008.

variables (velocity, pressure) and on the design variables which determine the geometry of the fluid filled domain. The state variables are supposed to satisfy the underlying fluid mechanical equations, and there are typically further technologically motivated constraints, e.g., bilateral constraints on the design variables which restrict the shape of the fluid filled domain to that what is technologically feasible.

Shape optimization problems have been extensively studied and are well documented in the literature (see, e.g., the monographs Allaire, 2002; Bendsøe, 1995; Bendsøe and Sigmund, 2003; Cherkaev, 2000; Delfour and Zolesio, 2001; Haslinger and Neittaanmäki, 1988; Haslinger and Mäkinen, 2004; Mohammadi and Pironneau, 2001; Pironneau, 1984; Rozvany, 1989; Sokolowski and Zolesio, 1992). The traditional approach relies on a separate treatment of the design objective and the state equation by an iterative cycle that starts from a given design, computes an approximate solution of the state equation for that design, invokes some sensitivity analysis for an update of the design, and continues this way until convergence is achieved. In contrast to this successive approximation, recently so-called 'all-at-once methods' or 'one-shot methods' have attracted considerable attention in PDE constrained optimization whose characteristic feature is that the numerical solution of the state equation is an integral part of the optimization routine. In particular, it has been shown that this novel approach may lead to significant savings of computational time (see, e.g., Biros and Ghattas, 2005a,b; Böhm et al., 2003; Hoppe, Linsenmann and Petrova, 2006; Hoppe and Petrova, 2004; Hoppe, Petrova and Schulz, 2002; Shenoy, Heinkenschloss and Cliff, 1998).

In this paper, we consider the optimal design of stationary fluid flow problems as described by the Stokes system. The objective is to design the geometry of a channel or a particular geometric feature of a channel such that a desired profile of the velocity and/or the pressure is realized as closely as possible. The design variables are chosen as the Bézier control points of a globally continuous Bézier curve representation of the walls of the channel. The control points are subject to bilateral constraints. For instance, for the shape optimization of a backward facing step (Fig. 1), we have used a moderate number m_1 of control points for the upper wall and $m_2 \gg m_1$ control points for the lower wall including the backward facing step.

The approach that we are pursuing here is an 'all-at-once method' based on a primal-dual formulation, where the Stokes system is coupled by Lagrange multipliers and the constraints on the design variables are taken care of by parameterized logarithmic barrier functions.
This leads to a family of minimization subproblems parameterized by the barrier parameter. The optimality conditions result in a parameter dependent nonlinear system, whose solution gives rise to the so-called central path (see, e.g., Forsgren, Gill and Wright, 2002; Wright, 1992). A significant challenge is to follow the central path as closely as possible as the barrier parameter goes to zero. Here, we use three path-following strategies. The first one is an adaptive

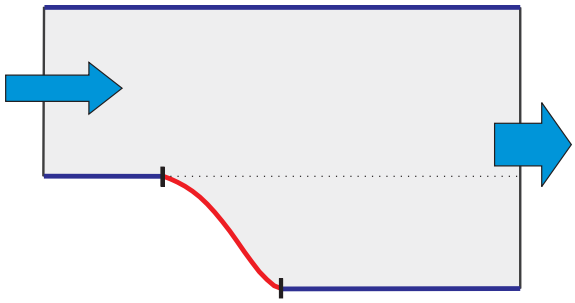

Figure 1. Channel with a backward facing step

continuation method with tangent continuation as a predictor and Newton's method as a corrector following the ideas from Deuflhard (2004), whereas the second and third ones are variants of the long-step target following algorithm and Mehrotra's algorithm known from linear programming (see, e.g., Wright, 1997). We note that path-following algorithms for shape optimization problems in structural mechanics have been used in Herskovits et al. (2000).

2. The shape optimization problem

We consider Stokes flow in a bounded domain $\Omega(\alpha) \subset \mathbb{R}^2$ with boundary $\Gamma(\alpha) = \Gamma_{in}(\alpha) \cup \Gamma_{lat}(\alpha) \cup \Gamma_{out}(\alpha)$, depending on the design variables $\alpha = (\alpha_1, \cdots, \alpha_m)^T \in \mathbb{R}^m$ which are chosen as the Bézier control points of a Bézier curve representation of the lateral boundaries of the domain. Denoting the viscosity of the fluid by ν, the velocity by $\mathbf{u}$ and the pressure by p, we refer to

$$J(\mathbf{u}, p, \alpha) := \frac{\kappa_1}{2} \int\limits_{\Omega(\alpha)} |\mathbf{u} - \mathbf{u}^d|^2 \, dx + \frac{\kappa_2}{2} \int\limits_{\Omega(\alpha)} |p - p^d|^2 \, dx$$

as the objective functional, where $\mathbf{u}^d, p^d$ are desired velocity and pressure profiles, and $\kappa_\nu, 1 \leq \nu \leq 2$, are appropriately chosen weighting factors. The shape optimization problem reads

$$\text{minimize } J(\mathbf{u}, p, \alpha) \tag{2.1}$$

subject to the Stokes system (state equations)

$$-\nabla \cdot \boldsymbol{\sigma}(\mathbf{u}) = 0 \quad \text{in } \Omega(\alpha), \tag{2.2a}$$

$$\nabla \cdot \mathbf{u} = 0 \quad \text{in } \Omega(\alpha),$$

$$\boldsymbol{\sigma}(\mathbf{u}) = -p\,\mathbf{I} + g(\mathbf{u}, \mathbf{D}(\mathbf{u}))\mathbf{D}(\mathbf{u}) \;, \tag{2.2b}$$

$$\mathbf{n} \cdot \mathbf{u} = \begin{cases} u_{in} & \text{on } \Gamma_{in}(\alpha) \\ 0 & \text{on } \Gamma_{lat}(\alpha) \end{cases} \;, \tag{2.2c}$$

$$\mathbf{t} \cdot \mathbf{u} = 0 \quad \text{on } \Gamma(\alpha) \;, \tag{2.2d}$$

where $\Gamma_{in}(\alpha), \Gamma_{lat}(\alpha)$ stand for the inflow and lateral boundaries with $\mathbf{n}, \mathbf{t}$ denoting the exterior unit normal vector and the tangential unit vector, respectively, and subject to the bilateral constraints

$$\alpha_i^{min} \ \leq \ \alpha_i \ \leq \ \alpha_i^{max} \ , \ 1 \leq i \leq m \tag{2.3}$$

on the design variables. It is well-known that the the weak formulation of (2.2a)-(2.2d) admits a unique solution (see, e.g., Litvinov, 2000).

We note that in the constitutive equation (2.2b) the tensor $\mathbf{D}(\mathbf{u})$ stands for the rate of deformation tensor $\mathbf{D}(\mathbf{u}) := (\nabla\mathbf{u} + (\nabla\mathbf{u})^T)/2$ and $g(\mathbf{u}, \mathbf{D}(\mathbf{u}))$ denotes the viscosity function which is given by $g(\mathbf{u}, \mathbf{D}(\mathbf{u})) = 2\nu$ for linear Stokes flow and depends nonlinearly on $\mathbf{u}, \mathbf{D}(\mathbf{u})$ in the nonlinear regime.

For the finite element approximation of (2.1)-(2.3) we choose $\hat{\alpha} \in K$ as a reference design and refer to $\hat{\Omega} := \Omega(\hat{\alpha})$ as the associated reference domain. Then, the actual domain $\Omega(\alpha)$ can be obtained from the reference domain $\hat{\Omega}$ by means of a mapping $\Omega(\alpha) = \Phi(\hat{\Omega}; \alpha)$. The advantage of using the reference domain $\hat{\Omega}$ is that finite element approximations can be performed with respect to that fixed domain without being forced to remesh for every new set of the design variables.

For the discretization of the velocity $\mathbf{u}$ and the pressure p, we use Taylor-Hood P2/P1 elements (see, e.g., Brezzi and Fortin, 1991) with respect to a shape regular family of simplicial triangulations of $\hat{\Omega}$ (Fig. 2 displays the finite element mesh for the final design of the channel with a backward facing step).

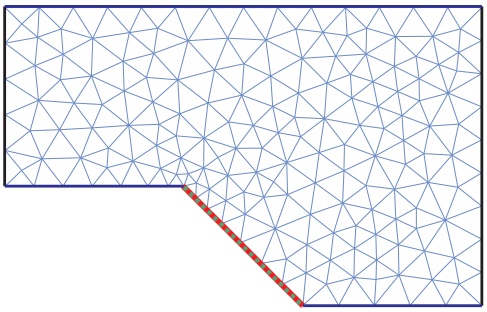

Figure 2. Finite element mesh for the optimal design of a channel with a backward facing step

We denote by $\mathbf{u}_h \in \mathbb{R}^{n_1}$ and $p_h \in \mathbb{R}^{n_2}$ the vectors standing for the velocity components and the pressure in the nodal points associated with the Taylor-Hood finite element approximation of the Stokes system, and we refer to $J_h(\mathbf{u}_h, p_h, \alpha)$ as the discretized objective functional. Then, the discrete optimal design problem can be stated as follows:

$$\text{minimize } J_h(\mathbf{u}_h, p_h, \alpha) \tag{2.4}$$

subject to the algebraic system (discretized Stokes equations)

$$S_h(\alpha)\mathbf{y}_h \;:=\; \begin{pmatrix} A_h(\mathbf{u}_h,\alpha) & B_h^T(\alpha) \\ B_h(\alpha) & 0 \end{pmatrix} \begin{pmatrix} \mathbf{u}_h \\ p_h \end{pmatrix} = \mathbf{g}_h, \tag{2.5}$$

where $\mathbf{y}_h := (\mathbf{u}_h, p_h)^T$ and $A_h(\mathbf{u}_h,\alpha) \in \mathbb{R}^{n_1\times n_1}, B_h(\alpha) \in \mathbb{R}^{n_2\times n_1}$, and further subject to the inequality constraints

$$\alpha_i^{min} \;\le\; \alpha_i \;\le\; \alpha_i^{max}\;,\; 1 \le i \le m. \tag{2.6}$$

Due to the nonlinear dependence on the design variables, (2.4)-(2.6) represents an inequality constrained nonlinear programming problem. It will be numerically solved by path-following primal-dual interior-point methods as described in the next section. For ease of notation, in the sequel we will drop the subindex h.

3. Path-following interior-point methods

We couple the inequality constraints (2.3) by logarithmic barrier functions with a barrier parameter $\beta = 1/\mu > 0$, $\mu \to \infty$, and the PDE constraint (2.2) by a Lagrange multiplier $\boldsymbol{\lambda} = (\boldsymbol{\lambda}_{\mathbf{u}}, \lambda_p)^T$. This leads to the saddle point problem

$$\inf_{\mathbf{y},\alpha} \sup_{\boldsymbol{\lambda}} L^{(\mu)}(\mathbf{y},\boldsymbol{\lambda},\alpha)\;, \tag{3.1}$$

where $L^{(\mu)}$ stands for the Lagrangian

$$L^{(\mu)}(\mathbf{y},\boldsymbol{\lambda},\alpha) \;=\; B^{(\mu)}(\mathbf{y},\alpha) \;+\; \langle S(\mathbf{y},\alpha) - \mathbf{g}, \boldsymbol{\lambda}\rangle\;, \tag{3.2}$$

and $B^{(\mu)}(\mathbf{y},\alpha)$ is the so-called barrier function as given by

$$B^{(\mu)}(\mathbf{y},\alpha) \;:= \tag{3.3}$$
$$J(\mathbf{y},\alpha) \;-\; \frac{1}{\mu}\sum_{i=1}^{m}[\ln(\alpha_i - \alpha_i^{\min}) + \ln(\alpha_i^{\max} - \alpha_i)]$$

(for details see, e.g., Wright, 1992).
The central path $\mu \longmapsto x(\mu) := (\mathbf{y}(\mu), \boldsymbol{\lambda}(\mu), \alpha(\mu))^T$ is given as the solution of the nonlinear system

$$F(x(\mu),\mu) \;=\; \begin{pmatrix} L_{\mathbf{y}}^{(\mu)}(\mathbf{y},\boldsymbol{\lambda},\alpha) \\ L_{\boldsymbol{\lambda}}^{(\mu)}(\mathbf{y},\boldsymbol{\lambda},\alpha) \\ L_{\alpha}^{(\mu)}(\mathbf{y},\boldsymbol{\lambda},\alpha) \end{pmatrix} \;=\; 0\;, \tag{3.4}$$

where the subindices refer to the derivatives of the Lagrangian with respect to the primal, the dual, and the design variables. The choice of the barrier parameter strongly influences the performance of the interior-point method.

There are static strategies with the Fiacco-McCormick approach as the most prominent one (Fiacco and McCormick, 1990), where the barrier parameter is fixed until an approximate solution of (3.1) has been obtained, and there is a variety of dynamic update strategies (see Armand, Benoist and Orban, 2007; El-Bakry et al., 1996; Gay, Overton and Wright, 1998; Nocedal, Wächter and Waltz, 2006; Tits et al., 2003; Ulbrich, Ulbrich and Vicente, 2004; Vanderbei and Shanno, 1999). Convergence properties of the Fiacco-McCormick approach have been studied in Byrd, Gilbert and Nocedal (2000) and Wächter and Biegler (2005), whereas a convergence analysis of dynamic update strategies has been addressed in Armand, Benoist and Orban (2007), El-Bakry et al. (1996), Nocedal, Wächter and Waltz (2006), Ulbrich, Ulbrich, and Vicente (2004).

We consider the solution of (3.4) by an adaptive continuation method based on the affine invariant convergence theory of Newton-type methods and nonlinear variants of the long-step and Mehrotra's path-following method (see Mehrotra, 1992).

3.1. Adaptive continuation method

The adaptive continuation method is a predictor-corrector method with an adaptively determined continuation step size in the predictor and Newton's method as a corrector. It relies on the affine invariant convergence theory of Newton and Newton-type methods (see, e.g., Deuflhard, 2004) and ensures that the iterates stay within a neighborhood (contraction tube) of the central path so that convergence to a local minimum of the original minimization problem can be achieved (Fig. 3).

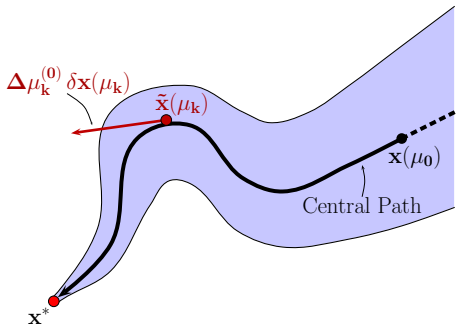

Figure 3. Predictor step of the adaptive continuation method.

Predictor Step: The predictor step relies on tangent continuation along the trajectory of the Davidenko equation

$$F_{\mathbf{x}}(\mathbf{x}(\mu),\mu)\;\mathbf{x}'(\mu) \;=\; -F_{\mu}(\mathbf{x}(\mu),\mu) \tag{3.5}$$

and amounts to the implementation of an explicit Euler step: Given some approximation $\tilde{\mathbf{x}}(\mu_k)$ at $\mu_k > 0$, compute $\tilde{\mathbf{x}}^{(j_0)}(\mu_{k+1})$, where $\mu_{k+1} = \mu_k + \Delta\mu_k^{(j)}$, according to

$$F_x(\tilde{\mathbf{x}}(\mu_k), \mu_k)\ \delta\mathbf{x}(\mu_k) \ = \ - \ F_\mu(\tilde{\mathbf{x}}(\mu_k), \mu_k)\ , \tag{3.6a}$$

$$\tilde{\mathbf{x}}^{(j_0)}(\mu_{k+1}) \ = \ \tilde{\mathbf{x}}(\mu_k) \ + \ \Delta\mu_k^{(j)}\ \delta\mathbf{x}(\mu_k)\ , \tag{3.6b}$$

starting with $j = 0$ ($j \geq 1$ only if required by the correction step (see below)). We use $\Delta\mu_0^{(0)} = \Delta\mu_0$ for some given initial step size $\Delta\mu_0$, whereas for $k \geq 1$ the predicted step size $\Delta\mu_k^{(0)}$ is chosen by

$$\Delta\mu_k^{(0)} \ := \tag{3.7}$$
$$\Big(\frac{\|\Delta\mathbf{x}^{(j_0)}(\mu_k)\|}{\|\tilde{\mathbf{x}}(\mu_k) - \tilde{\mathbf{x}}^{(j_0)}(\mu_k)\|}\ \frac{\sqrt{2}-1}{2\Theta(\mu_k)}\Big)^{1/2}\ \Delta\mu_{k-1}\ ,$$

where $\Delta\mu_{k-1}$ is the computed continuation step size, $\Delta\mathbf{x}^{(j_0)}(\mu_k)$ is the first Newton correction (see below), and $\Theta(\mu_k) < 1$ is the contraction factor associated with a successful previous continuation step.

Corrector step: As a corrector, we use Newton's method applied to $F(\mathbf{x}(\mu_{k+1}), \mu_{k+1}) = 0$ with $\tilde{\mathbf{x}}^{(j_0)}(\mu_{k+1})$ from (3.6) as a start vector. In particular, for $\ell \geq 0$ (Newton iteration index) and $j_\ell \geq 0$ (j being the steplength correction index) we compute $\Delta\mathbf{x}^{(j_\ell)}(\mu_{k+1})$ according to

$$F_x(\tilde{\mathbf{x}}^{(j_\ell)}(\mu_{k+1}), \mu_{k+1})\ \Delta\mathbf{x}^{(j_\ell)}(\mu_{k+1}) \ = \tag{3.8}$$
$$-\ F(\tilde{\mathbf{x}}^{(j_\ell)}(\mu_{k+1}), \mu_{k+1})\ ,$$

update $\tilde{\mathbf{x}}^{(j_{\ell+1})}(\mu_{k+1}) := \tilde{\mathbf{x}}^{(j_\ell)}(\mu_{k+1}) + \Delta\mathbf{x}^{(j_\ell)}(\mu_{k+1})$ and compute $\overline{\Delta\mathbf{x}}^{(j_\ell)}(\mu_{k+1})$ as the associated simplified Newton correction

$$F_x(\tilde{\mathbf{x}}^{(j_\ell)}(\mu_{k+1}), \mu_{k+1})\ \overline{\Delta\mathbf{x}}^{(j_\ell)}(\mu_{k+1}) \ = \tag{3.9}$$
$$-\ F(\tilde{\mathbf{x}}^{(j_\ell)}(\mu_{k+1}) + \Delta\mathbf{x}^{(j_\ell)}(\mu_{k+1}), \mu_{k+1})\ .$$

We monitor convergence of Newton's method by means of

$$\Theta^{(j_\ell)}(\mu_{k+1}) \ := \ \|\overline{\Delta\mathbf{x}}^{(j_\ell)}(\mu_{k+1})\| / \|\Delta\mathbf{x}^{(j_\ell)}(\mu_{k+1})\|\ .$$

In case of successful convergence, we set $\tilde{\mathbf{x}}(\mu_{k+1}) := \tilde{\mathbf{x}}^{(j_\ell)}(\mu_{k+1})$ with ℓ being the current Newton iteration index, accept the current step size $\Delta\mu_k := \Delta\mu_k^{(j)}$ with current steplength correction index j and proceed with the next continuation step. However, if the monotonicity test

$$\Theta^{(j_\ell)}(\mu_{k+1}) \ < \ 1 \tag{3.10}$$

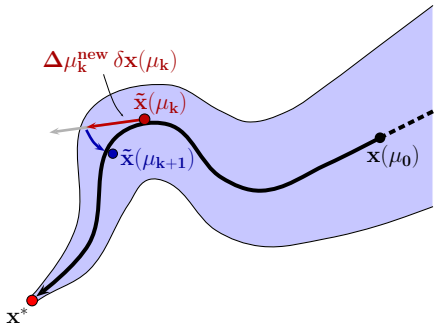

Figure 4. Correction step of the adaptive continuation method.

fails for some $j_\ell \geq 0$, the predicted steplength $\Delta\mu_k^{(j)}$ has been chosen too large so that the predicted solution $\tilde{\mathbf{x}}^{(j_0)}(\mu_{k+1})$ is not situated within the Kantorovich neighborhood of $\mathbf{x}(\mu_{k+1})$, i.e., it is outside the contraction tube around the central path (see Fig. 4). The corrector step provides a correction of the steplength for the tangent direction $\delta\mathbf{x}(\mu_k)$ such that the new iterate stays within the contraction tube. To do so, the continuation step from (3.6b) has to be repeated with the reduced step size

$$\begin{aligned} \Delta\mu_k^{(j+1)} &:= \left(\frac{\sqrt{2}-1}{g(\Theta^{(j_\ell)})}\right)^{1/2} \Delta\mu_k^{(j)}\ , \\ g(\Theta) &:= \sqrt{\Theta+1}-1, \end{aligned} \tag{3.11}$$

until we either achieve convergence or for some prespecified lower bound $\Delta\mu_{min}$ observe

$$\Delta\mu_k^{(j+1)} \ < \ \Delta\mu_{min}\ .$$

In the latter case, we stop the algorithm and report convergence failure.

The Newton steps are realized by an inexact Newton method featuring right-transforming iterations (see, e.g., Hoppe, Linsenmann and Petrova, 2006, Hoppe and Petrova, 2004). The derivatives occurring in the KKT conditions and the Hessians are computed by automatic differentiation (see, e.g., Griewank, 2000) based on the automatic differentiation package from the INTLAB toolbox (see Rump, 1999).

3.2. Long-step path-following method

The long-step path-following method is based on the formulation of the KKT system with respect to the auxiliary variables $\mathbf{z} = (z_1, z_2)^T$ given by

$$\begin{aligned} z_{1,i} &:= \frac{1}{\mu\ (\alpha_i - \alpha_i^{\min})}\ , \\ z_{2,i} &:= \frac{1}{\mu\ (\alpha_i^{\max} - \alpha_i)} \quad , \quad 1 \leq i \leq m\ , \end{aligned} \tag{3.12}$$

which are referred to as perturbed complementarity. A Newton step in the increments

$$\Delta x \;:=\; (\Delta\mathbf{y}, \Delta\boldsymbol{\lambda}, \Delta\alpha, \Delta\mathbf{z})^T$$

reads as follows (for notational convenience, in the following the upper index (μ) in the Lagrangian will be dropped):

$$\begin{pmatrix} M_\kappa(\alpha) & \boldsymbol{\nabla} S(\alpha) & L_{\mathbf{y},\alpha} & 0 \\ \boldsymbol{\nabla} S(\alpha) & 0 & L_{\boldsymbol{\lambda},\alpha} & 0 \\ L_{\alpha,\mathbf{y}} & L_{\alpha,\boldsymbol{\lambda}} & L_{\alpha,\alpha} & \hat{I} \\ 0 & 0 & \hat{Z} & D \end{pmatrix} \begin{pmatrix} \Delta\mathbf{y} \\ \Delta\boldsymbol{\lambda} \\ \Delta\alpha \\ \Delta\mathbf{z} \end{pmatrix} \;=\; -\tilde{\mathbf{g}} \;. \tag{3.13}$$

Here, $L_{\mathbf{y},\alpha}$ etc. stand for the second derivatives of the Lagrangian and

$$M_\kappa(\alpha) := \mathrm{diag}(\kappa_1 M_1(\alpha), \kappa_2 M_2(\alpha)) \;,\; \hat{I} := (-I, I) \;,$$
$$\hat{Z} := (Z_1, -Z_2)^T \;,\; D := \mathrm{diag}(D_1, D_2) \;,$$
$$\tilde{\mathbf{g}} := (\mathbf{g}, D_1 Z_1 e - \sigma\mu^{-1} e, D_2 Z_2 e - \sigma\mu^{-1} e)^T \;,$$

where M_1, M_2 denote the velocity and pressure mass matrices, $Z_1 := \mathrm{diag}(z_{1,i})$, $Z_2 := \mathrm{diag}(z_{2,i})$, $D_1 := \mathrm{diag}(\alpha_i - \alpha_i^{min})$, $D_2 := \mathrm{diag}(\alpha_i^{max} - \alpha_i)$, $e := (1, 1, \cdots, 1)^T$ and $\sigma > 0$ stands for the centering parameter.

We define $\mathcal{N}_{-\infty}(\gamma), 0 < \gamma \ll 1$, as the following neighborhood of the central path

$$\mathcal{N}_{-\infty}(\gamma) := \{(\mathbf{y}, \boldsymbol{\lambda}, \alpha, \mathbf{z}) \mid \mathbf{s}_\alpha^T \mathbf{z} \geq \mu^{-1}\gamma\} \;, \tag{3.14}$$

where $\mathbf{s}(\alpha) := (s_1(\alpha), s_2(\alpha))^T, s_1(\alpha) := \alpha - \alpha^{min}, s_2(\alpha) := \alpha^{max} - \alpha$.
The long-step path-following algorithm proceeds as follows:

Initialization: Specify $0 < \gamma \ll 1$, bounds $0 < \sigma_{min} < \sigma_{max} < 1$ for the centering parameter, and choose a start iterate

$$\mathbf{x}^{(0)} = (\mathbf{y}^{(0)}, \boldsymbol{\lambda}^{(0)}, \alpha^{(0)}, \mathbf{z}^{(0)}) \in \mathcal{N}_{-\infty}(\gamma) \;.$$

Iteration loop: For $k = 0, 1, 2, \ldots$ set

$$\mu^{(k)} := \max\left(\frac{m}{(s_1^{(k)})^T z_1^{(k)}}, \frac{m}{(s_2^{(k)})^T z_2^{(k)}}\right) \tag{3.15}$$

where $s_\nu^{(k)} := s_\nu(\alpha^{(k)}), 1 \leq \nu \leq 2$.
Choose $\sigma_k \in (\sigma_{min}, \sigma_{max})$, and compute

$$\Delta\mathbf{x}^{(k)} = (\Delta\mathbf{y}^{(k)}, \Delta\boldsymbol{\lambda}^{(k)}, \Delta\alpha^{(k)}, \Delta\mathbf{z}^{(k)})$$

as the solution of (3.13). Set

$$\begin{aligned} \mathbf{x}^{(k+1)} &:= \mathbf{x}^{(k)} + \eta_k \Delta\mathbf{x}^{(k)} \;, \\ \eta_k &:= \max\{\eta \in (0,1) \mid \mathbf{x}^{(k)} + \eta\Delta\mathbf{x}^{(k)} \in \mathcal{N}_{-\infty}(\gamma)\} \;. \end{aligned}$$

Given a tolerance tol, the iteration will be terminated, if for some $k^* \geq 1$

$$|J(\mathbf{y}^{(k^*)}, \alpha^{(k^*)}) - J(\mathbf{y}^{(k^*-1)}, \alpha^{(k^*-1)})| \ < \ tol \ .$$

For $k \geq 1$, a possible choice of the centering parameter $\sigma^{(k)}$ is $\sigma^{(k)} := \left(\mu^{(k-1)}/\mu^{(k)}\right)^2$.

The solution of (3.13) is computed based on static condensation of the slack variables and the application of right-transforming iterations to the resulting reduced Hessian system (see, e.g., Hoppe, Linsenmann and Petrova, 2006; Hoppe and Petrova, 2004) using INTLAB for automatic differentiation.

3.3. Nonlinear version of Mehrotra's method

Using the same notation as in subsection 3.2, the nonlinear version of Mehrotra's method (see Mehrotra, 1992) is as follows:

Initialization: Choose a start iterate

$$\mathbf{x}^{(0)} = (\mathbf{y}^{(0)}, \boldsymbol{\lambda}^{(0)}, \alpha^{(0)}, \mathbf{z}^{(0)}) \ .$$

Iteration loop: For $k = 0, 1, 2, \ldots$ define $\mu^{(k)}$ as in (3.15) and solve (3.13) with $\sigma = 0$ for

$$(\Delta\mathbf{y}^{aff}, \Delta\boldsymbol{\lambda}^{aff}, \Delta\alpha^{aff}, \Delta\mathbf{z}^{aff})^T.$$

Compute

$$\begin{aligned}
\beta^p_{aff} &:= \max\{\beta \in (0,1) \mid \alpha^{(k)} + \beta\Delta\alpha^{aff} \geq 0\}, \\
\beta^d_{aff} &:= \max\{\beta \in (0,1) \mid \mathbf{z}^{(k)} + \beta\Delta\mathbf{z}^{aff} \geq 0\}, \\
\mu_{aff} &:= \max_{1\leq\nu\leq 2} \frac{m}{(s^{(k)}_\nu + \beta^p_{aff}\Delta\alpha^{aff})^T(\mathbf{z}^{(k)}_\nu + \beta^d_{aff}\Delta\mathbf{z}^{aff}_\nu)} \ , \\
\sigma^{(k)} &:= (\mu^{(k)}/\mu_{aff})^3.
\end{aligned}$$

Solve (3.13) for $(\Delta\mathbf{y}^{(k)}, \Delta\boldsymbol{\lambda}^{(k)}, \Delta\alpha^{(k)}, \Delta\mathbf{z}^{(k)})^T$ with right-hand side $\tilde{\mathbf{g}}$ replaced by

$$\begin{aligned}
\hat{\mathbf{g}} \ := \ (&\mathbf{g}, D_1Z_1e + \Delta D_1\Delta Z_1e - \sigma^{(k)}(\mu^{(k)})^{-1}e, \\
&D_2Z_2e + \Delta D_2\Delta Z_2e - \sigma^{(k)}(\mu^{(k)})^{-1}e)^T \ ,
\end{aligned}$$

where

$$\begin{aligned}
\Delta D_1 \ &:= \ \mathrm{diag}(\alpha^{(k)}_i + \beta^p_{aff} \ \Delta\alpha^{aff}_i - \alpha^{min}_i) \ , \\
\Delta D_2 \ &:= \ \mathrm{diag}(\alpha^{max}_i - (\alpha^{(k)}_i + \beta^p_{aff} \ \Delta\alpha^{aff}_i)) \ , \\
\Delta Z_\nu \ &:= \ \mathrm{diag}(\Delta\mathbf{z}^{aff}_\nu) \ .
\end{aligned}$$

Set

$$\begin{aligned}
\bar{\beta}_k^p &:= \max\{\beta \in \mathbb{R}_+ \mid \alpha^{(k)} + \beta \Delta\alpha^{(k)} \geq 0\} \ , \\
\bar{\beta}_k^d &:= \max\{\beta \in \mathbb{R}_+ \mid z^{(k)} + \beta \Delta\mathbf{z}^{(k)} \geq 0\} \ , \\
\beta_k^p &:= \max\{0.99 \cdot \bar{\beta}_k^p, 1) \quad , \quad \beta_k^d := \max\{0.99 \cdot \bar{\beta}_k^d, 1) \ ,
\end{aligned}$$

and compute a new iterate $\mathbf{x}^{(k+1)}$ according to

$$\begin{aligned}
(\mathbf{y}^{(k+1)}, \alpha^{(k+1)}) &= (\mathbf{y}^{(k)}, \alpha^{(k)}) + \beta_k^p (\Delta\mathbf{y}^{(k)}, \Delta\alpha^{(k)}) \ , \\
(\boldsymbol{\lambda}^{(k+1)}, \mathbf{z}^{(k+1)}) &= (\boldsymbol{\lambda}^{(k)}, \mathbf{z}^{(k)}) + \beta_k^d (\Delta\boldsymbol{\lambda}^{(k)}, \Delta\mathbf{z}^{(k)}) \ .
\end{aligned}$$

The termination criterion is the same as in the long-step path-following method.

4. Applications

4.1. Channel with a backward facing step

As a benchmark problem, we consider linear Stokes flow in a channel with a backward facing step (see Fig. 1). The initial shape (straight line) and the optimal shape (dotted line) with regard to a desired velocity field according to prespecified design $\bar{\alpha}$ are shown in Fig. 5. Here, the three horizontal segments of the geometry are fixed and only the segment that connects the two lower horizontal segments is variable. In this setting, the function that describes the bottom segment of the geometry is a composite Bézier curve consisting of three curves of degree 0, 4 and 0, respectively. Note that the composite curve is only continuous. The data for this geometry are as follows

$$\begin{aligned}
&\hat{\Omega} = \Omega(\bar{\alpha}),\ \bar{\alpha} = (+1.0, -0.5, -0.5, -1.5, -1.5, -1.5)^T, \\
&\alpha^0 = (+1.0, -0.5, -0.55, -0.6, -0.6, -1.5)^T, \\
&\nu = 1.0 \ , \ u_{in}(x_1, x_2) = (6(1 + x_2)(1 - x_2),\ 0)^T, \\
&\alpha^{min} = (0, -5, -5, -5, -5, -5)^T, \\
&\alpha^{max} = (5, 0, 0, 0, 0, 0)^T.
\end{aligned}$$

The problem has been solved using the adaptive continuation method as described in Subsection 3.1. Table 1 reflects the convergence history of the iterative process. Here, the columns labeled J and Θ contain the actual values of the objective functional and the contraction factor in the monotonicity test, respectively.

Fig. 6 displays the velocity field (top) and the pressure distribution (bottom) for the computed optimal shape.

The adaptive continuation method has been compared with the dynamic barrier update strategy from Gay, Overton and Wright (1998), which was also used in Hoppe, Linsenmann and Petrova (2006), Hoppe and Petrova (2004),

Table 1. Backward facing step: convergence history of the adaptive continuation method

k	μ	$\Delta\mu$	J	Θ
0	1.0E+02	3.0E+02	2.63E+00	–
1	1.0E+02	3.0E+02	9.32E-01	0.58
			3.30E-01	0.61
			2.42E-01	0.83
			1.08E-02	–
2	2.7E+02	1.7E+02	1.94E-04	0.32
			4.17E-06	0.73
			2.47E-05	0.09
3	3.6E+02	9.8E+01	1.15E-05	0.01
4	3.7E+02	3.9E+02	6.68E-07	–

Table 2. Backward facing step: comparison adaptive continuation method (ACM), dynamic barrier update strategy (DBUS) from Gay, Overton and Wright (1998) and Mehrotra's method (MEHR) on a coarse mesh ($h_{max} = 0.3$)

Method	Cont. Steps	J	Exec. Time
ACM	4	6.68E-07	5 min
DBUS	8	9.32E-07	8 min
MEHR	–	no conv.	–

Table 3. Backward facing step: comparison adaptive continuation method (ACM), dynamic barrier update strategy (DBUS) from Gay, Overton and Wright (1998) and Mehrotra's method (MEHR) on a finer mesh ($h_{max} = 0.1$)

Method	Cont. Steps	J	Exec. Time
ACM	3	4.98e-07	59 min
DBUS	11	9.42e-07	142 min
MEHR	8	6.61e-07	34 min

and the nonlinear variant of Mehrotra's path-following method. For these three methods, Tables 2 and 3 contain the number of continuation steps, the final value of the objective functional, and the execution time on a coarse mesh ($h_{max} = 0.3$) and on a finer mesh ($h_{max} = 0.1$), where 'no conv.' means no convergence. The results show that the adaptive continuation method is more efficient than the dynamic barrier update strategy and more robust than Mehrotra's method for which convergence only occurs, if the mesh is fine enough. On the other hand, for this robustness one has to pay a price in terms of the execution time (see Table 3).

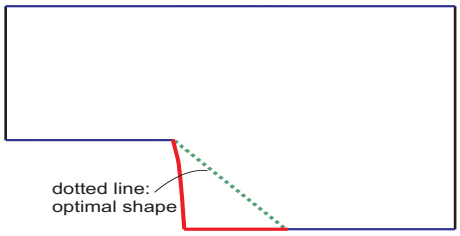

Figure 5. Initial and optimal shape of the backward facing step.

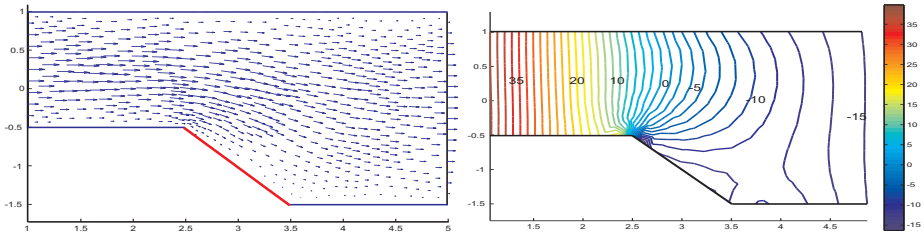

Figure 6. Velocity field (top) and pressure distribution (bottom) associated with the optimal shape.

4.2. Capillary barrier

Programmable microfluidic biochips and microarrays are used in pharmaceutical, medical and forensic applications as well as in academic research and development for high throughput screening, genotyping and sequencing by hybridization in genomics, protein profiling in proteomics, and cytometry in cell analysis (see Pollard and Castrodale, 2003). They are miniaturized biochemical labs that are physically and/or electronically controllable and guarantee a precise positioning of the samples (e.g., DNA solutes or proteins) on the surface of the chip. Recent technology uses Surface Acoustic Wave (SAW) driven microfluidic biochips whose operating principle is based on piezoelectrically actuated surface acoustic waves on the surface of a chip which transport the droplet containing probe along a lithographically produced network to reservoirs at prespecified surface locations serving as miniaturized chemical labs. They allow the in-situ investigation of the dynamics of hybridization processes with extremely high time resolution (see, e.g., Wagner et al., 2002; Wixforth, Scriba and Gauer, 2002). Fig. 7 gives an illustration of such a microfluidic biochip.
One of the issues in the optimal design of the biochips is to make sure that the reservoir is filled with a very precise amount of the probe containing liquid. This is taken care of by a capillary barrier placed between a channel and the reservoir (see Fig. 8).

The SAW induced fluid flow in the channels can be described by a multi-

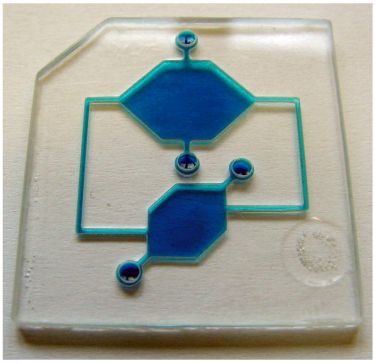

Figure 7. Surface Acoustic Wave (SAW) driven microfluidic biochip

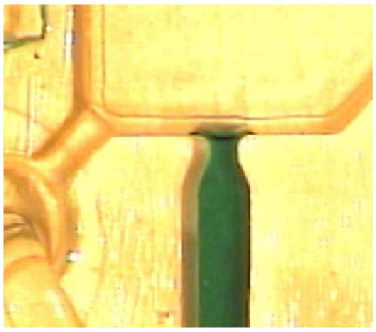

Figure 8. Channel with capillary barrier on an SAW driven microfluidic biochip

physics and multi-scale system consisting of the linearized equations of piezoelectricity coupled with the compressible Navier-Stokes equations. The induced fluid flow involves very different time scales. The SAWs enter the fluid filled channels within nanoseconds creating sharp jets in the fluid which get significantly damped while propagating along the channels. After a couple of milliseconds, a stationary flow pattern is formed, called acoustic streaming, which describes the transport of the probes within the network. Since the acoustic streaming can be modeled by stationary Stokes flow obtained by the application of appropriate homogenization techniques, the optimal design of the capillary barriers fits the framework set in this paper.

Mathematical models for SAW biochips are based on the linearized equations of piezoelectricity in $Q_1 := (0, T_1) \times \Omega_1$

$$\begin{aligned} \rho_1 \frac{\partial^2 u_i}{\partial t^2} - \frac{\partial}{\partial x_j} c_{ijkl} \frac{\partial u_k}{\partial x_l} - \frac{\partial}{\partial x_j} e_{kij} \frac{\partial \Phi}{\partial x_k} &= 0 \,, \\ \frac{\partial}{\partial x_j} e_{jkl} \frac{\partial u_k}{\partial x_l} - \frac{\partial}{\partial x_j} \epsilon_{jk} \frac{\partial \Phi}{\partial x_k} &= 0, \end{aligned}$$

with appropriate initial conditions at $t = 0$ and boundary conditions on $\Gamma_1 := \partial\Omega_1$. Here, ρ_1 and $\mathbf{u} = (u_1, u_2, u_3)^T$ denote the density of the piezoelectric material and the mechanical displacement vector. Moreover, $\boldsymbol{\epsilon} = (\epsilon_{ij})$ is the permittivity tensor and Φ stands for the electric potential. The tensors $\mathbf{c} = (c_{ijkl})$ and $\mathbf{e} = (e_{ikl})$ refer to the fourth order elasticity tensor and third-order piezoelectric tensor, respectively. The SAWs are excited by interdigital transducers located on top of the chip operating at a frequency $f \approx 100$ MHz with wavelength $\lambda \approx 40\ \mu m$. The modeling of the micro-fluidic flow relies on the compressible Navier-Stokes equations in $Q_2 := (0, T_2) \times \Omega_2$

$$\begin{aligned}
\rho_2\big(\frac{\partial \mathbf{v}}{\partial t} + (\mathbf{v}\cdot\nabla)\mathbf{v}\big) &= -\nabla p + \eta\Delta\mathbf{v} + \big(\zeta + \frac{\eta}{3}\big)\nabla(\nabla\cdot\mathbf{v}),\\
\frac{\partial \rho_2}{\partial t} + \nabla\cdot(\rho_2\ \mathbf{v}) &= 0,\\
\mathbf{v}(x + \mathbf{u}(x,t), t) &= \frac{\partial \mathbf{u}}{\partial t}(x,t) \quad \text{on } (0,T_2)\times\Gamma_2
\end{aligned}$$

with suitable initial conditions at $t = 0$. Compressible and nonlinear effects are the driving force of the resulting flow. Here, $\rho_2, \mathbf{v} = (v_1, v_2, v_3)^T$ and p are the density of the fluid, the velocity, and the pressure. η and ζ refer to the shear and the bulk viscosity. The boundary conditions include the time derivative $\partial\mathbf{u}/\partial t$ of the displacement of the walls $\Gamma_2 = \partial\Omega_2$ of the microchannels caused by the surface acoustic waves. The induced fluid flow involves extremely different time scales. The penetration of the acoustic waves into the fluid-filled channels represents a process with a time scale of nanoseconds, whereas the resulting acoustic streaming is achieved on a time scale of milliseconds. In order to cope with the two time-scales character of the fluid flow in the microchannels, we perform a separation of the time-scales by homogenization. We consider an expansion of the velocity $\mathbf{v}$ in a scale parameter $\varepsilon > 0$ representing the maximum displacement of the walls

$$\mathbf{v} \;=\; \mathbf{v}_0 \;+\; \varepsilon\ \mathbf{v}' \;+\; \varepsilon^2\ \mathbf{v}'' \;+\; O(\varepsilon^3)$$

and analogous expansions of the pressure p and the density ρ_2. We set $\mathbf{v}_1 := \varepsilon\mathbf{v}', \mathbf{v}_2 := \varepsilon^2\mathbf{v}''$ and define $p_i, \rho_{2,i}$ for $1 \le i \le 2$ analogously. Collecting all terms of order $O(\varepsilon)$ results in the linear system

$$\begin{aligned}
&\rho_{2,0}\frac{\partial \mathbf{v}_1}{\partial t} - \eta\Delta\mathbf{v}_1 - \Big(\zeta + \frac{\eta}{3}\Big)\nabla(\nabla\cdot\mathbf{v}_1) + \nabla p_1 = \mathbf{0} \text{ in } Q_2,\\
&\frac{\partial \rho_{2,1}}{\partial t} + \rho_{2,0}\nabla\cdot\mathbf{v}_1 = \mathbf{0} \text{ in } Q_2,\\
&p_1 = c_0^2\rho_{2,1} \text{ in } Q_2 \quad , \quad \mathbf{v}_1 = \frac{\partial \mathbf{u}}{\partial t} \text{ on } \Gamma_2.
\end{aligned}$$

Here, c_0 stands for the small signal sound speed in the fluid. The system describes the propagation of the damped acoustic waves in the channel. Collecting all terms of order $O(\varepsilon^2)$ and performing the time-averaging $\langle w\rangle :=$

$T^{-1}\int_{t_0}^{t_0+T} w\,dt$, where $T := 2\pi/\omega$, we arrive at the following Stokes system

$$\begin{aligned} -\eta\,\Delta\mathbf{v}_2 - \Big(\zeta + \frac{\eta}{3}\Big)\nabla(\nabla\cdot\mathbf{v}_2) + \nabla p_2 \;&= \\ &= \langle -\rho_{2,1}\frac{\partial \mathbf{v}_1}{\partial t} - \rho_{2,0}[\nabla\mathbf{v}_1]\mathbf{v}_1\rangle \text{ in } \Omega_2\ , \\ \rho_{2,0}\nabla\cdot\mathbf{v}_2 \;&= \langle -\nabla\cdot(\rho_{2,1}\mathbf{v}_1)\rangle \text{ in } \Omega_2\ , \\ \mathbf{v}_2 \;&= -\ \langle[\nabla\mathbf{v}_1]\mathbf{u}\rangle \text{ on } \Gamma_2\ . \end{aligned}$$

The Stokes system describes the stationary flow pattern, called acoustic streaming, resulting after the relaxation of the high frequency surface acoustic waves. For more details we refer to Antil et al. (2007), Gantner et al. (2007), Köster (2007).

The Stokes system has been used as the state equation for the optimal design of a capillary barrier. As computational domain we have chosen a part of a channel with a capillary barrier at its end and a part of a reservoir connected with the channel by the capillary barrier. In the objective functional, we have chosen $\kappa_1 = \kappa_2 = 1$ and $\mathbf{u}^d, p^d$ based on information provided by Olympus Medical Systems Europe GmbH (2007). The problem has been discretized by P2/P1 Taylor-Hood elements. For the shape optimization we have applied all three methods described in section 3 using a Bézier curve representation of the barrier. Fig. 9 displays the computed optimal shape of the barrier together with an underlying finite element mesh. The channel, in addition, has passive outlet valves (see Fig. 9) that are activated when the barrier operates in stopping mode and back flow occurs.

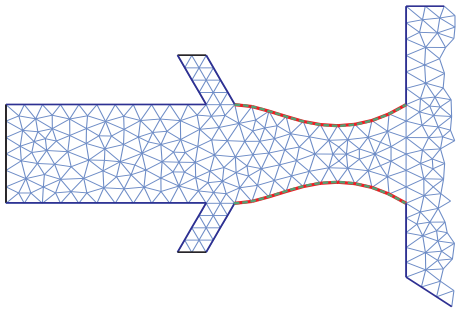

Figure 9. Optimal shape of the capillary barrier and underlying finite element mesh

Fig. 10 provides a visualization of the velocity field for the optimized channel under conditions of flow from the channel into the reservoir.

Likewise, Fig. 11 displays the velocity field for the optimized channel under back flow conditions, i.e., when the capillary barrier operates in stopping mode.

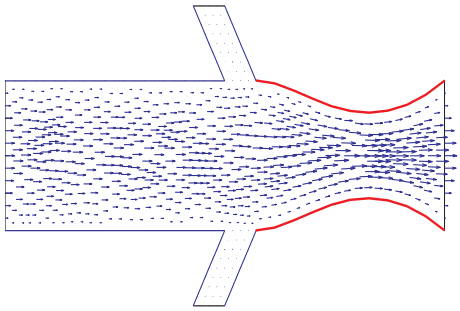

Figure 10. Velocity field for the optimal configuration when the barrier is not in stopping mode

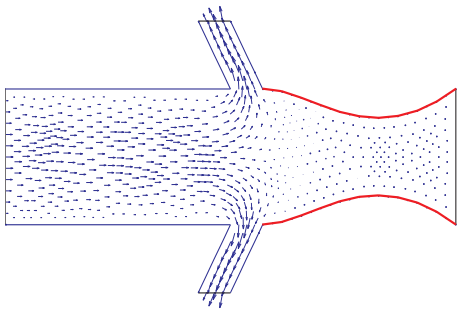

Figure 11. Velocity field (back flow) for the optimal configuration when the barrier is in stopping mode

We compared the adaptive continuation method with the long-step path-following algorithm and Mehrotra's algorithm. As in the previous example, we observed robustness of the adaptive continuation method in so far as it converges on relatively coarse meshes where the two other algorithms fail to converge. Below we report the convergence history and execution times of all three algorithms for a sufficiently fine finite element mesh with a total of $N_{dof} = 62916$ degrees of freedom. We used 16 Bézier control points for the Bézier curve representation of the capillary barrier as design variables and a tolerance $tol = 1.0E-03$ as termination criterion. Tables 4, 5 and 6 display the convergence histories of the three algorithms.

4.3. Electrorheological shock absorbers

Electrorheological shock absorbers are based on electrorheological fluids (ERF) which are suspensions of small electrically polarizable particles dissolved in non-conducting liquids such as silicon oils. Under the influence of an outer electric

Table 4. Capillary barrier: convergence history of the adaptive continuation method

k	μ	$\Delta\mu$	ΔJ	Time
0	2.0E+02	5.0E+02	–	
1	6.9E+02	4.9E+02	2.83E+00	
2	1.2E+03	5.3E+02	4.58E-05	747 min

Table 5. Capillary barrier: convergence history of the long-step path following method

k	μ	σ	η	ΔJ	Time
0	2.0E+02	–	–	–	
1	2.0E+02	1.0E-03	1	2.35E+00	
2	3.2E+03	1.2E-01	1	4.80E-01	
3	9.2E+03	7.2E-03	1	5.34E-04	360 min

Table 6. Capillary barrier: convergence history of Mehrotra's method

k	μ	σ	β^p, β^d	ΔJ	Time
0	2.0E+02	–	–	–	
1	2.0E+02	1.0E-05	0.99	2.37E+00	
2	3.2E+03	4.1E-02	0.99	4.62E-01	
3	1.2E+03	1.4E-07	0.99	5.04E-04	371 min

field the particles form chains along the electric field lines and then aggregate to form larger and larger columns thus changing the viscosity of the fluid. This is called the electrorheological effect which happens within a few milliseconds and is reversible. Due to the electrorheological effect, ERF are used in all technological processes where a controlled power transmission plays a significant role such as automotive shock absorbers (see Filisko, 1995). Fig. 12 (left) gives a schematic representation of an ERF absorber which consists of two fluid chambers connected by small ducts within the piston. The walls of the ducts serve as the electrodes, and the power supply is guaranteed by an external source connected to the electrodes through the piston rod.

An important optimization issue is to design the inflow and outflow boundaries of the ducts both in the compression mode (piston is moving down) and in the rebound mode (piston is moving up) such that pressure peaks are avoided which may cause inappropriate damping profiles. This amounts to the solution of a pressure tracking problem. The state equations are based on the equations of

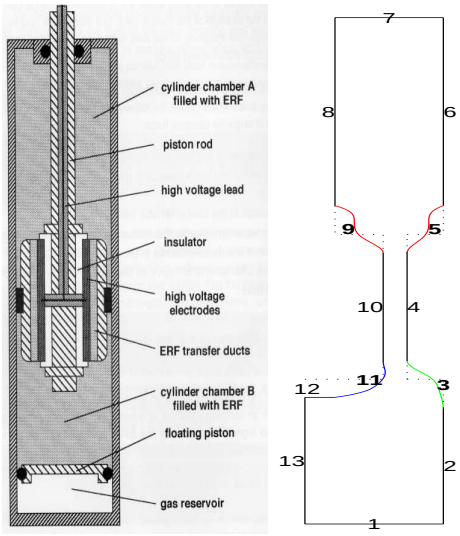

Figure 12. Electrorheological shock absorber: schematic diagram (left) and Bézier curve representation of the inlet and outlet boundaries of the right part of the fluid chamber (right)

motion for an incompressible ERF

$$\rho\,(\frac{\partial \mathbf{u}}{\partial t} + (\mathbf{u}\cdot\nabla)\,\mathbf{u}) - \nabla\cdot\boldsymbol{\sigma}(\mathbf{u}) \;=\; \mathbf{f} \quad \text{in } Q\,, \tag{4.1}$$

$$\nabla\cdot\mathbf{u} \;=\; 0 \quad \text{in } Q\,, \tag{4.2}$$

where $Q := \Omega\times(0,T)$, along with appropriate boundary conditions and an initial condition (see below). Here, ρ stands for the density of the ERF, $\mathbf{u} = (u_1, u_2)$ is the velocity vector, $\boldsymbol{\sigma}$ refers to the stress tensor and $\mathbf{f}$ describes exterior forces acting on the fluid. The stress tensor $\boldsymbol{\sigma}$ is related to the rate of the deformation tensor $(\mathbf{D}(\mathbf{u}))_{ij} := (\partial u_i/\partial x_j + \partial u_j/\partial x_i)/2\ ,\ 1 \le i,j \le 2$, by a constitutive equation where the electric field $\mathbf{E}$ enters as a parameter

$$\boldsymbol{\sigma} \;=\; -p\,\mathbf{I} \;+ 2\,\varphi(I(\mathbf{u}), |\mathbf{E}|, \mu(\mathbf{u},\mathbf{E}))\;\mathbf{D}(\mathbf{u})\;. \tag{4.3}$$

Note that φ is a viscosity function depending on the shear rate $I(\mathbf{u})$, the electric field strength $|\mathbf{E}|$, and the angle $\mu(\mathbf{u},\mathbf{E})$ between the velocity field $\mathbf{u}$ and the electric field $\mathbf{E}$. We refer to Hoppe and Litvinov (2004), Hoppe, Litvinov and Rahman (2003) for details.

Due to the geometry of the shock absorber, the fluid flow is assumed to be axially symmetric so that the computational domain can be restricted to the right half of the fluid chamber and displayed in the cylindrical coordinates r, z. Caused by the displacement $a(t)$ of the piston, the computational domain

changes in time and will thus be denoted by $\Omega_{a(t)}$. If the piston is displaced by $a(t) = l_1(t) - l_1(0)$, the floating piston is displaced from its initial position by $b(t) = a(t)(R_1/R)^2$, where R and R_1 are the radii of the floating piston and the piston rod. For a proper specification of the boundary conditions, we refer to $\Gamma_{a(t)} = \partial\Omega_{a(t)}$ as the boundary of the right half of the fluid chamber. In particular, $\Gamma^{(p)}_{a(t)}$ and $\Gamma^{(f)}_{a(t)}$ stand for the boundary of the piston and the upper boundary of the floating piston. We further denote by $\Gamma^{(e)}_{a(t)}$ and $\Gamma^{(c)}_{a(t)}$ the inner wall and the outer wall of the transfer duct, which serve as the electrode and counter electrode, respectively. Finally, $\Gamma^{(\ell)}_{a(t)} := \{(r,z) \in \overline{\Omega}_{a(t)} \mid r = 0\}$ stands for the left boundary of the computational domain, which coincides with the symmetry axis. We set $Q := \Omega_{a(t)} \times (0,T), \Sigma_{a(t)} := \Gamma_{a(t)} \times (0,T)$ and use analogous notations for the other space-time domains involving the specific parts of the boundary of the computational domain. Taking advantage of the axial symmetry, the velocity $\mathbf{u}$ is given by

$$\mathbf{u}(r,z) \;=\; u_1(r,z)e_r \;+\; u_2(r,z)e_z \;,$$

which gives rise to the following components of the strain tensor

$$\begin{aligned}
&\varepsilon_{11}(\mathbf{u}) \;=\; \frac{\partial u_1}{\partial r} \quad , \quad \varepsilon_{22}(\mathbf{u}) \;=\; \frac{u_1}{r} \quad , \quad \varepsilon_{33}(u) \;=\; \frac{\partial u_2}{\partial z} \;, \\
&\varepsilon_{13}(\mathbf{u}) \;=\; \varepsilon_{31}(u) \;=\; \frac{1}{2}\Big(\frac{\partial u_1}{\partial z} + \frac{\partial u_2}{\partial z}\Big) \;, \\
&\varepsilon_{12}(\mathbf{u}) \;=\; \varepsilon_{21}(\mathbf{u}) \;=\; \varepsilon_{23}(\mathbf{u}) \;=\; \varepsilon_{32}(\mathbf{u}) \;=\; 0 \;.
\end{aligned}$$

The second invariant of the rate of strain tensor turns out to be

$$I(\mathbf{u}) \;=\; \Big(\frac{\partial u_1}{\partial r}\Big)^2 \;+\; \Big(\frac{u_1}{r}\Big)^2 \;+\; \Big(\frac{\partial u_2}{\partial z}\Big)^2 \;+\; \frac{1}{2}\Big(\frac{\partial u_1}{\partial z} + \frac{\partial u_2}{\partial r}\Big)^2 \;.$$

Denoting by $\mathbf{f} = (f_1, f_2)^T$ the volume force with the radial and axial components f_1 and f_2, the equations of motion take the form

$$\begin{aligned}
&\rho\Big(\frac{\partial u_1}{\partial t} + u_1\frac{\partial u_1}{\partial r} + u_2\frac{\partial u_1}{\partial z}\Big) + \frac{\partial p}{\partial r} - 2\frac{\partial}{\partial r}(\varphi\ \varepsilon_{11}(\mathbf{u})) - \\
&- 2\frac{\partial}{\partial z}(\varphi\ \varepsilon_{13}(\mathbf{u})) - \frac{2}{r}\varphi\ (\varepsilon_{11}(\mathbf{u}) - \varepsilon_{22}(\mathbf{u})) \;=\; f_1, \\
&\rho\Big(\frac{\partial u_2}{\partial t} + u_1\frac{\partial u_2}{\partial r} + u_2\frac{\partial u_2}{\partial z}\Big) + \frac{\partial p}{\partial r} - \\
&-\; 2\frac{\partial}{\partial r}(\varphi\ \varepsilon_{13}(\mathbf{u})) - 2\frac{\partial}{\partial z}(\varphi\ \varepsilon_{33}(\mathbf{u})) - \frac{2}{r}\varphi\ \varepsilon_{13}(\mathbf{u}) \;=\; f_2, \\
&\nabla\cdot\mathbf{u} \;=\; \frac{\partial u_1}{\partial r} + \frac{\partial u_2}{\partial z} + \frac{u_1}{r} \;=\; 0.
\end{aligned}$$

Moreover, referring to $v^{(p)}$ as the piston velocity and to $u^{(0)}$ as some given initial

velocity, the boundary conditions and the initial condition are given by

$$\begin{aligned}
u_1 &= 0 \qquad \text{on } \Sigma_{a(t)} \ , \\
u_2 &= v^{(p)} \quad \text{on } \Sigma^{(p)}_{a(t)} \ , \\
u_2 &= v^{(p)}(R_1/R)^2 \quad \text{on } \Sigma^{(f)}_{a(t)} \ , \\
u_2 &= 0 \qquad \text{on } \Sigma_{a(t)} \setminus (\overline{\Sigma}^{(f)}_{a(t)} \cup \overline{\Sigma}^{(\ell)}_{a(t)} \cup \overline{\Sigma}^{(p)}_{a(t)}) \ , \\
\frac{\partial u_2}{\partial r} &= 0 \qquad \text{on } \Sigma^{(\ell)}_{a(t)} \ , \\
\mathbf{u}(\cdot,0) &= \mathbf{u}^{(0)} \quad \text{in } \Omega_{a(t)} \ .
\end{aligned}$$

The motion of the piston satisfies the initial-value problem

$$\begin{aligned}
m \ \frac{dv^{(p)}}{dt}(t) &= g(t, v^{(p)}(t), U(t)) \quad , \quad t \in (0,T) \ , \\
v^{(p)}(0) &= v_0^{(p)} < 0 \ ,
\end{aligned}$$

where m is the sum of the mass of the piston and the mass of the body that strikes the piston at $t = 0$, $U(t)$ stands for the applied voltage, and the drag force g is given by

$$\begin{aligned}
&g(t, v^{(p)}(t), U(t)) \ := \\
&\qquad - \int\limits_{\Sigma^{(p)}_{a(t)}} \Big(2\varphi \ \varepsilon_{31}(\mathbf{u})\nu_r + (2\varphi \ \varepsilon_{33}(\mathbf{u}) - p)\nu_z \Big) \ ds \ .
\end{aligned}$$

The electric field E has the form

$$E(r,z) \ = \ E_1(r,z)e_r \ + \ E_2(r,z)e_z \ .$$

It can be computed by means of an electric potential $\psi(t)$ which at each time instant $t \in [0,T]$ satisfies the following elliptic boundary value problem

$$\begin{aligned}
\nabla \cdot (\epsilon \nabla \psi(t)) &= 0 \qquad \text{in } \Omega_{a(t)} \ , \\
\psi(t) &= U(t) \quad \text{on } \Gamma^{(e)}_{a(t)} \ , \\
\psi(t) &= 0 \qquad \text{on } \Gamma^{(c)}_{a(t)} \ , \\
\frac{\partial \psi}{\partial r}(t) &= 0 \qquad \text{on } \Gamma^{(\ell)}_{a(t)} \ , \\
\nu_r \epsilon \frac{\partial \psi}{\partial r}(t) + \nu_z \epsilon \frac{\partial \psi}{\partial z}(t) &= 0 \qquad \text{elsewhere} \ .
\end{aligned}$$

For the numerical simulation we have used a discretization in time with respect to a uniform partition of the time interval $[0,T]$ of step size $k := T/M$,

$M \in \mathbb{N}$, using the explicit Euler scheme for the equation of motion of the piston and the implicit Euler scheme for the equations of motion of the fluid with. The discretization in space has been taken care of by P_2/P_1 Taylor-Hood elements for the fluid variables and conforming P_1 elements for the electric potential with respect to a simplicial triangulation of $\Omega_{a(t_m)}$. The discretized fluid equations have been solved by an augmented Lagrangian algorithm, whereas the preconditioned conjugate gradient method has been used for the discretized potential equation.

At selected time instants t_1^* and t_2^* reflecting snapshots of the shock absorber in the rebound and compression mode, we have computed the optimal shape of the outlet boundary and inlet boundary, respectively, based on the primal-dual interior point method described in Section 3. We have chosen a pressure dominated tracking type objective functional, i.e., $\kappa_2 \gg \kappa_1$ in $J(\mathbf{u}, p, \alpha)$ from Section 2, with $\mathbf{u}^d$ and p^d specified based on information from the producer of ERF shock absorbers (Schenck Pegasus GmbH, 2007). The computed optimal shape of the outlet boundary in the rebound mode is shown in Fig. 13 for various applied electric field strengths.

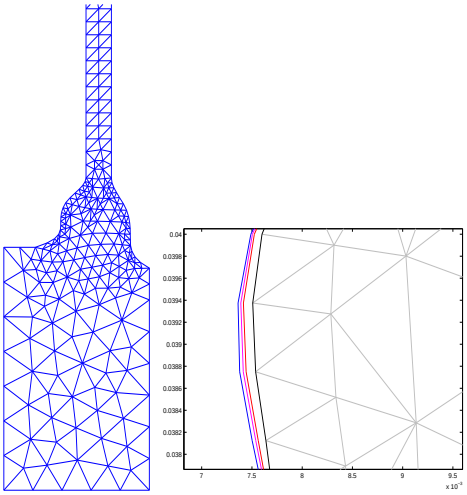

Figure 13. Optimized outlet boundary (left) and details of the optimal design for various electric field strengths (right)

5. Conclusions

We have provided an 'all-at-once approach' for the optimal design of stationary flow problems described by linear and nonlinear Stokes flow featuring path-following primal-dual interior-point methods by means of an adaptive predictor-corrector type continuation method, a long-step path-following algorithm and

a nonlinear version of Mehrotra's algorithm. The computation of the first order derivatives in the KKT systems and the second order derivatives in the Hessians is significantly facilitated by automatic differentiation. Numerical examples including a benchmark problem and two real-life design problems demonstrate that the methods can be used in shape optimization with the adaptive continuation method being the most robust algorithm at the expense of slightly higher execution times on finer finite element meshes.

References

Allaire, G. (2002) *Shape Optimization by the Homogenization Method*. Springer, Berlin-Heidelberg-New York.

Antil, H., Gantner, A., Hoppe, R.H.W., Köster, D., Siebert, K.G. and Wixforth, A. (2007) Modeling and Simulation of Piezoelectrically Agitated Acoustic Streaming on Microfluidic Biochips. In: U. Langer, et al., eds., *Proc. 17th Int. Conf. on Domain Decomposition Methods, Lecture Notes in Computational Science and Engineering*, **60**, Springer, Berlin Heidelberg-New York.

Armand, P., Benoist, J. and Orban, D. (2007) Dynamic updates of the barrier parameter in primal-dual methods for nonlinear programming. To appear in *Computational Optimization and Applications*.

Bendsøe, M.P. (1995) *Optimization of Structural Topology, Shape, and Material*. Springer, Berlin-Heidelberg-New York.

Bendsøe, M.P. and Sigmund, O. (2003) *Topology Optimization: Theory, Methods and Applications*. Springer, Berlin-Heidelberg-New York.

Biros, G. and Ghattas, O. (2005a) Parallel Lagrange-Newton-Krylov-Schur methods for PDE-constrained optimization. Part i: the Krylov-Schur solver. *SIAM J. Sci. Comp.* **27**, 687–713.

Biros, G. and Ghattas, O. (2005b) Parallel Lagrange-Newton-Krylov-Schur methods for PDE-constrained optimization. Part ii: the Lagrange-Newton solver and its application to optimal control of steady viscous flows. *SIAM J. Sci. Comp.* **27**, 714–739.

Böhm, P., Hoppe, R.H.W., Mazurkevitch, G., Petrova, S.I., Wachutka, G. and Wolfgang, E. (2003) Optimal structural design of high power electronic devices by topology optimization. In: Krebs H, and Jäger W (eds.), *Mathematics - Key Technology for the Future. Cooperations between Mathematics and Industry*, Springer, Berlin-Heidelberg-New York, 365–376.

Byrd, R.H., Gilbert, J.C. and Nocedal, J. (2000) A trust region method based on interior point techniques for nonlinear programming. *Math. Programming* **89**, 149–185.

Cherkaev, A. (2000) *Variational Methods for Structural Optimization*. Springer, New York.

Brezzi, F. and Fortin, M. (1991) *Mixed and Hybrid Finite Element Methods*. Springer, Berlin-Heidelberg-New York.

Byrd, R.H., Hribar, M.E. and Nocedal, J. (1999) An interior point algorithm for large scale nonlinear programming. *SIAM J. Optimization* **9**, 877–900.

Delfour, M.C. and Zolesio, J.P. (2001) *Shapes and Geometries: Analysis, Differential Calculus and Optimization*. SIAM, Philadelphia.

Deuflhard, P. (2004) *Newton Methods for Nonlinear Problems. Affine Invariance and Adaptive Algorithms*. Springer, Berlin-Heidleberg-New York.

El-Bakry, A.S., Tapia, R.A., Tsuchiya, T. and Zhang, Y. (1996) On the formulation and theory of the Newton interior-point method for nonlinear programming. *JOTA* **89**, 507–541.

Fiacco, A.V. and McCormick, G.P. (1990) *Nonlinear Programming: Sequential Unconstrained Minimization Techniques*. SIAM, Philadelphia.

Filisko, F. (1995) Overview of ER technology. In: K. Havelka (ed.), *Progress in ER Technology*, Plenum Press, New York.

Forsgren, A., Gill, Ph.E. and Wright, M.H. (2002) Interior methods for nonlinear optimization. *SIAM Rev.* **44**, 522–597.

Gantner, A., Hoppe, R.H.W., Köster, D., Siebert, K.G. and Wixforth, A. (2007) Numerical simulation of piezoelectrically agitated surface acoustic waves on microfluidic biochips. *Comp. Visual. Sci.* DOI 10.1007/s00791-006-0040-y (in press).

Gay, D.M., Overton, M.L. and Wright, M.H. (1998) A primal-dual interior method for nonconvex nonlinear programming. In: Y. Yuan, ed., *Advances in Nonlinear Programming*, Kluwer, Dordrecht, 31–56.

Griewank, A. (2000) *Evaluating Derivatives, Principles and Techniques of Automatic Differentiation*. SIAM, Phildelphia.

Haslinger, J. and Neittaanmäki, P. (1988) *Finite Element Approximation for Optimal Shape Design: Theory and Applications*. John Wiley & Sons, Chichester.

Haslinger, J. and Mäkinen, R.A.E. (2004) *Introduction to Shape Optimization: Theory, Approximation, and Computation*. SIAM, Philadelphia.

Herskovits, J., Dias, G., Santos, G. and Mota Soares, C.M. (2000) Shape structural optimization with an interior point nonlinear programming algorithm. *Struct. Multidisc. Optim.* **20**, 107–115.

Hoppe, R.H.W., Linsenmann, C. and Petrova, S.I. (2006) Primal-dual Newton methods in structural optimization. *Comp. Visual. Sci.* **9**, 71–87.

Hoppe, R.H.W. and Litvinov, W.G. (2004) Problems on electrorheological fluid flows. *Communications in Pure and Applied Analysis* **3**, 809–848.

Hoppe, R.H.W., Litvinov, W.G. and Rahman, T. (2003) Mathematical modeling and numerical simulation of electrorheological devices and systems. In: P. Neittaanmäki and O. Pironneau (eds.), *Proc. Int. Conf. on Scientific Computing, Jyväskylä, Finland, June 14/15, 2002*, CIMNE, Barcelona, 80–93.

Hoppe, R.H.W. and Petrova, S.I. (2004) Primal-dual Newton interior-point methods in shape and topology optimization. *Numer. Linear Algebra Appl.* **11**, 413–429.

Hoppe, R.H.W., Petrova, S.I. and Schulz, V. (2002) A primal-dual Newton-type interior-point method for topology optimization. *Journal of Optimization: Theory and Applications* **114**, 545-571.

Köster, D. (2007) Numerical simulation of acoustic streaming on SAW-driven biochips. *SIAM J. Comp. Sci.* **29**, 2352–2380.

Litvinov, W.G. (2000) *Optimization in Elliptic Problems with Applications to Mechanics of Deformable Bodies and Fluid Mechanics.* Birkhäuser, Basel.

Mehrotra, S. (1992) On the implementation of a primal-dual interior point method. *SIAM J. on Optimization* **2**, 575–601.

Mohammadi, B. and Pironneau, O. (2001) *Applied Shape Optimization for Fluids.* Oxford University Press, Oxford.

Nocedal, J., Wächter, A. and Waltz, R.A. (2006) Adaptive barrier update strategies for nonlinear interior methods. *Research Report* RC 23563, IBM T. J. Watson Research Center, Yorktown.

Olympus Medical Systems Europe GmbH (2007) Private communication.

Pironneau, O. (1984) *Optimal Shape Design for Elliptic Systems.* Springer, Berlin-Heidelberg-New York.

Pollard, J. and Castrodale, B. (2003) Outlook for DNA microarrays: emerging applications and insights on optimizing microarray studies. Report. Cambridge Health Institute, Cambridge.

Rozvany, G. (1989) *Structural Design via Optimality Criteria.* Kluwer, Dordrecht.

Rump, S.M. (1999) INTLAB - INTerval LABoratory. In: T. Csendes, ed., *Developments in Reliable Computing*, Kluwer, Dordrecht, 77–106.

Schenck Pegasus GmbH (2007) Private communication.

Shenoy, A.R., Heinkenschloss, M. and Cliff, E.M. (1998) Airfoil design by an all-at-once approach. *Int. J. Comput. Fluid Mechanics* **11**, 3–25.

Sokolowski, J. and Zolesio, J.P. (1992) *Introduction to Shape Optimization.* Springer, Berlin-Heidelberg-New York.

Tits, A.L., Wächter, A., Bakhtiari, S., Urban, T.J. and Lawrence, C.T. (2003) A primal-dual interior-point method for nonlinear programming with strong global and local convergence properties. *SIAM J. on Optimization* **14**, 173–199.

Ulbrich, M., Ulbrich, S. and Vicente, L. (2004) A globally convergent primal-dual interior point filter method for nonconvex nonlinear programming. *Math. Programming* **100**, 379–410.

Vanderbei, R.J. and Shanno, D.F. (1999) An interior point algorithm for nonconvex nonlinear programming. *Computational Optimization and Applications* **13**, 231–252.

Wächter, A. and Biegler, L.T. (2005) Line search filter methods for nonlinear programming: motivation and global convergence. *SIAM J. on Optimization* **16**, 1–31.

Wagner, P., Tan, M.X., Zaugg, F.G. and Indermühle, P.F. (2002) Protein biochips: protein analysis on a small scale. *mst news* **5**, 44.

Wittum, G. (1989) On the convergence of multigrid iterations with transforming smoothers. Theory with applications to the Navier-Stokes equations. *Numer. Math.* **57**, 15-38.

Wixforth, A., Scriba, J. and Gauer, G. (2002) Flatland fluidics. *mst news* **5**, 42-43.

Wright, M.H. (1992) Interior methods for constrained optimization. *Acta Numerica* **1**, 341-407.

Wright, S.J. (1997) *Primal-Dual Interior-Point Methods.* SIAM, Philadelphia.